A multiscale modelling approach to elucidate the mechanism of the oxygen evolution reaction at the hematite-water interface

Sinha, V.; Sun, D.; Meijer, E. J.; Vlugt, T. J.H.; Bieberle-Hutter, A.

DOI
10.1039/c9fd00140a

Publication date
2021

Document Version
Accepted author manuscript

Published in
Faraday Discussions

A Multiscale Modelling Approach to Elucidate the Mechanism of the Oxygen Evolution Reaction at the Hematite-Water Interface

V. Sinha[*1,2], D. Sun[3], E. J. Meijer[3], T. J. H. Vlugt[*2], A. Bieberle-Hütter[*1]

[1] Electrochemical Materials and Interfaces, Dutch Institute for Fundamental Energy Research (DIFFER), de Zaale 20, 5612 AJ, Eindhoven, The Netherlands

[2] Process and Energy Department, Faculty of Mechanical, Maritime and Materials Engineering, Delft University of Technology, Leeghwaterstraat 39, 2628CB, Delft, The Netherlands

[3]Amsterdam Center for Multiscale Modelling and van' t Hoff Institute for Molecular Sciences, University of Amsterdam, Amsterdam, The Netherlands.

* corresponding authors: V.Sinha@differ.nl, T.J.H.Vlugt@tudelft.nl, A.Bieberle@differ.nl

Abstract

Photoelectrochemical (PEC) splitting of water to make hydrogen is a promising clean-energy technology. Oxygen evolution reaction (OER) largely determines the energy efficiency in PEC water-splitting. Hematite, which is a cheap and sustainable semiconductor material with excellent chemical properties, a favourable band gap (2.1 eV) and composed of earth abundant elements is a suitable model photoanode material for studying OER. To understand the design of energy efficient anodes, it is highly desirable to have mechanistic insight in OER at an atomistic level which can be directly connected to experimentally measured quantities. We present a multiscale computational model of OER which connects the thermodynamics and kinetics of elementary charge transfer reactions in OER to kinetics of OER at laboratory length and time scales. We couple density functional theory (DFT) and DFT based molecular dynamics (DFT-MD) simulations with solvent effects at an atomistic level with kinetic Monte Carlo (kMC) simulations at a coarse-grained level in our multiscale model. The time and applied bias potential dependent surface coverage, which are experimentally not known, and the O_2 evolution rate during OER at the hematite-water interface are calculated by the multiscale model. Furthermore, the multiscale model demonstrates the effect of explicitly modelling the interaction of water with the electrode surface via direct adsorption.

Introduction

Reversible storage of energy from sunlight in chemical bonds is a promising strategy towards a sustainable clean-energy economy.[1] Photoelectrochemical (PEC) cells which produce hydrogen by splitting water into hydrogen and oxygen (water-splitting reaction) under solar illumination are of high interest in this regard. PEC water-splitting consists of two main events: the hydrogen evolution reaction (HER) which produces hydrogen on the cathode ($2H^+(aq) + 2e^- \rightarrow H_2(g), E^0_{cathode} = 0$ V), and the oxygen evolution reaction (OER) where oxygen gas is produced on the anode ($2H_2O(l) \rightarrow 4H^+(aq) + O_2(g) + 4e^-, E^0_{anode} = 1.23$ V). The OER includes a transfer of four electrons and protons which makes it energetically challenging, and a main contributor to the overall energy efficiency of the PEC cell.[2] Therefore, the design of energy efficient anode materials for the OER is important in order to develop highly active PEC cells.

Recent research efforts have been directed towards identifying catalysts based on earth abundant metals such as W, Fe, Ti, Zn, V to make their application sustainable in the energy economy.[3] Among these materials, hematite (α-Fe_2O_3) has emerged as a promising photoanode for PEC splitting of water due to its suitable band gap of about 2.1 eV, an excellent chemical stability, its natural abundance, nontoxicity, and low cost.[3] However, issues such as high overpotential and short diffusion length limit the efficiency and the overall benefits of hematite.[3] Both advantages and disadvantages together make hematite a particularly interesting model photoanode material. Mechanistic insight derived from both experimental and computational studies have paved the way for the development of a manifold of strategies, such as use of transition metal (TM) dopants,[4] fabrication of nanostructures,[5] engineering co-catalyst interfaces,[6] introducing O vacancies[7], to reduce the electrochemical overpotential. However, there are still significant opportunities in improving the catalytic activity of hematite towards OER.

At a microscopic level, water is oxidized to O_2 via electrochemical transformations that occur at the surface of the anode which is in direct contact with water. Therefore, the elementary steps in the OER occur at a solid-liquid interface. On the macroscopic level, say at the laboratory length and time scales, OER is characterized by polarization curves (current density vs applied bias potential (V)) and electrochemical impedance spectra. It is therefore desirable to be able to connect the electrochemical transformations at the atomistic scale to experimentally measured data. A detailed mechanistic insight can help in identifying the limiting processes during

the charge-transfer events and present nanoscale design/engineering opportunities to improve the overall energy efficiency of PEC cells. Recently, some experimental efforts have resulted in mechanistic insight into OER over hematite under the operando conditions. For example, Zandi and Hamman used operando infrared spectroscopy to study the mechanism of OER over hematite and observed formation of an Fe^{IV}=O intermediate during the OER.[8a] Durrant et al. used photoinduced absorption spectroscopy to study the rate law for PEC OER at hematite and reported a third order dependence of OER kinetics on the concentration of surface holes.[8b] Such experimental measurements are highly desirable, since they reveal atomistic insights under operando conditions which can be directly/indirectly correlated with indicators of catalytic acidity for OER. However, these experiments are extremely challenging and sometimes even impossible due to the dynamic and highly sensitive nature of the electrochemical transformations at the solid-liquid interface. In this regard, multiscale computational models which connect the thermodynamics and kinetics of the elementary steps at the atomistic level to the activity at laboratory scale and which can simulate electrochemical measurements, are of high interest.[2,9] From a molecular perspective, this requires an electrochemical model which can provide the rate constants for elementary transformations at the solid-liquid interface as a function of the operando conditions.

An electrochemical model that can compute the rate constants, necessitates a detailed investigation of the thermodynamics and the kinetics of the elementary steps in the OER at the hematite-water interface under the operando conditions. The operando conditions elicit incorporation of the interaction of intermediates with *V*, solvent effects, photo-illumination, pH, surface coverage and the resultant adsorbate-adsorbate interactions etc. in the electrochemical model. A complete examination of a multitude of such interactions is beyond the scope of this manuscript. We focus our investigation on elucidating the effect of solvent in modelling the thermodynamics and kinetics of elementary reactions in the OER at the solid-liquid interface in the presence of *V*. Since OER occurs at the solid-liquid interface, interaction of intermediates with the solvent molecules is an important quantity from a mechanistic perspective. A complete examination of solvent effects needs the following investigations: a) effect of solvation on the thermodynamic stability of intermediates involved in the elementary reactions b) transition state barriers for transfer of charge (H^+/e^-) from surface species at the solid-liquid interface.

Most computational studies of OER over hematite have studied the elementary reactions in OER using Density Functional Theory (DFT) calculations. These calculations typically use a solid-gas interface to simulate OER due to the large computational cost associated with explicitly modelling the solid-liquid interface.[7,14,15] However, solvent effects can also play an important role by selectively influencing the stability of one intermediate with respect to others, and in turn have an effect on the rate constants and the overpotential. The importance of solvent effects on the thermodynamic stability of intermediates has been discussed in the literature in the context of oxygen reduction reaction (ORR; reverse of OER) and OER for various metals and metal oxides such as Pt(111), IrO_2 etc.[10] Some recent studies have also performed detailed investigations of the hematite-water interface and the related acidity constants at the interface.[11,12] However, to the best of our knowledge such studies have not been performed in the context of OER on Fe_2O_3 surfaces. The impact of solvent on the relative stabilities of intermediates in OER can be operational either by direct hydrogen bonding interactions or via the dielectric constant of the solvent or both. To include hydrogen bonding effects with the solvent one needs to model the solvent environment in an explicit manner which can be computationally expensive. The impact of dielectric constant of the solvent can be modelled by using a linearized Poisson−Boltzmann equation, and modelling the solvent in an implicit manner as a polarizable dielectric continuum, for example by using VASPsol[13,24] as implemented in VASP.[21]

In addition to thermodynamic stabilities, calculation of the transition state (TS) barriers for proton transfer reactions from surface adsorbed intermediates is highly desirable. Having computed the thermodynamic stabilities of intermediates and the TS barriers for proton transfer, one can then use an electrochemical model to compute the rate constant for electrochemical steps as a function of applied potential.[14b] Computation of TS barriers for proton transfer from surface adsorbed species is a central problem in estimating the rate constants for electrochemical steps in OER. Various computational studies have computed the TS barrier for proton transfer from various surface species during OER/ORR on different metal/metal oxide surfaces.[14,15c] However, to the best of our knowledge TS barriers for proton transfer reactions from intermediates in the OER over hematite have not been computed so far. Moreover, these studies have considered a single solvation layer and as such omit complete solvation and temperature effects which can be important for an accurate description of the dynamics of the solid-liquid interface.

In this study, we present a multiscale model to study the mechanism of OER. DFT calculations with solvent effects are used to elucidate the thermodynamic stabilities of intermediates in OER. We limit our examination of the solvent effects to an implicit solvation model via VASPsol. Explicit solvent effects can also be important for the thermodynamic stabilities and it is a topic of ongoing research. We apply DFT-MD simulations to estimate the TS barriers for proton transfer from intermediates formed during OER. Our investigations are limited to

computing the TS barrier for proton transfer (TS_{H^+}) from a surface adsorbed water moiety (H_2O^*; * denotes surface adsorbed species). A complete elucidation of TS_{H^+} involving OH*, O* and OOH* species will be published separately at a later stage. Interaction of H_2O with the reactive site of hematite is a pre-requirement for OER to proceed. Very often, DFT based mechanistic studies omit an explicit modelling of the adsorption of water over the catalyst surface although some recent studies have accounted explicitly for this step.[15] This neglect of solvent effect via explicit adsorption over the catalyst surface can affect the overpotential for OER as suggested recently in a combined spectroscopic and DFT study.[16] Using our multiscale model we outline the importance of modelling the adsorption of water on the reaction mechanism.

The manuscript is organized as follows: we first describe the reaction mechanism, computational model and the computational methods. Next, we present and discuss our results from DFT, DFT-MD, kMC simulations and the multiscale model. Finally, we summarize the results and present our conclusions with an outlook on future research towards further developing the multiscale model of OER.

Reaction Mechanism, Computational Model, and Methods

Reaction Mechanism: We look at two related mechanisms of OER: **M1** and **M2** (Table 1). Mechanism **M1** involves five elementary steps: one thermochemical step (eq.(1)) and four electrochemical steps (eq.(2) – (5)). Carter et al. also used **M1** to study the OER on the hematite 0001 surface.[15a] The first step in the mechanism **M1** is thermochemical adsorption of water at the active site to form H_2O^*. Next, H_2O^* undergoes deprotonation and $1e^-$ oxidation (proton coupled electron transfer, PCET) to form OH^* species with production of a H^+/e^- pair at the hematite-water interface. The following PCET event converts OH^* to O^*. Simultaneous addition of a water molecule and a PCET event converts the O^* species to OOH^*. In the final step, OOH^* undergoes PCET to release the fourth and the final H^+/e^- pair and evolves O_2 gas.

Table 1: Elementary steps considered in the mechanism of OER within mechanism **M1** and **M2**.

M1		**M2**	
$* + H_2O(l) \rightarrow H_2O^*$	(1)	$H_2O(l) + * \rightarrow OH^* + H^+ + e^-$	(2′)
$H_2O^* \rightarrow OH^* + H^+ + e^-$	(2)	$OH^* \rightarrow O^* + H^+ + e^-$	(3)
$OH^* \rightarrow O^* + H^+ + e^-$	(3)	$O^* + H_2O(l) \rightarrow OOH^* + H^+ + e^-$	(4)
$O^* + H_2O(l) \rightarrow OOH^* + H^+ + e^-$	(4)	$OOH^* \rightarrow O_2 + H^+ + e^-$	(5)
$OOH^* \rightarrow O_2 + H^+ + e^-$	(5)		

The mechanism **M1** is a slightly extended version of the four-step PCET mechanism (**M2**) for OER as proposed by Rossmeisl and co-workers.[17] Mechanism (**M2**) only involves four elementary steps which are all electrochemical in nature and omits the thermochemical adsorption of water. We have omitted the desoprtion of O_2 which is a thermochemical step from the mechanism because of the known difficulties in accurately describing the electronic structure/energy of O_2^* adduct and the transition state barrier for its desorption reliably with GGA level of theory in DFT.[15c] We assume that the thermochemical adsorption of water is not significantly affected by *V* since it does not involve production of any charged species at the hematite-water interface. The electrochemical steps produce charged species (H^+/e^-) at the electrode-electrolyte interface and therefore will be directly affected by the applied potential which is elaborated further in the next section.

Computational Model: This section describes the computational model used in this manuscript. The energy of $\mathbf{H^+ + e^-}$ produced in the electrochemical steps in OER is calculated by taking the reference potential to be standard hydrogen electrode (SHE). Then, the chemical potential of $\mathbf{H^+ + e^-}$ equals that of 0.5 H_2 in the gas phase i.e. the free energy of $\mathbf{H^+ + e^-}$ equals the free energy of 0.5 H_2 at $p = 1\ atm, pH = 0, T = 298\ K$.[18] The effect of *V* on all electrochemical steps (i.e. eq(2) – eq(5)) which release an electron in the electrode is included by shifting the corresponding Gibbs free energy by $\Delta G_i(V) = \Delta G_i\ (0) - eV,\ i = \{2,3,4,5\}$ where $\Delta G_i(V)$ is the Gibbs free energy of the reaction *i*.[18] Therefore, when $V = 0$, the reaction steps 2 – 5 are equivalent to reactions producing 0.5 equivalent of molecular dihydrogen e.g. eq(2) is equivalent to $H_2O^* \rightarrow OH^* + 0.5H_2$. The effect of pH on the Gibbs free energy of the electrochemical steps is modelled by including the term $-kT \cdot \ln(10) \cdot pH$ term in the Gibbs free energy. Furthermore, the Gibbs free energy values include zero point energy (ZPE) correction and entropy contribution (TΔS) ($F_{i,i\in[1,5]}$ denotes the combined correction for ZPE - TΔS; these corrections are taken from reference-15b). The total Gibbs free energy of the OER is fixed at the experimental value (4.92 eV) for the reaction $2H_2O \rightarrow O_2 + 2H_2$ that is:

$$\Delta G_1 + \Delta G_2 + \Delta G_3 + \Delta G_4 + \Delta G_5 = 4.92\ \text{eV}.^{18} \quad (6)$$

This is done to avoid computing the energy O_2 using DFT with a GGA functional which is erroneous in accurately describing the electronic structure and energy of O_2.[18]

Overall, the Gibbs free energy of all of the steps at pH = 0 can be written as:

$$\Delta G_1 = E_{H_2O^*} - E_* - E_{H_2O} + F_1 \quad (7)$$
$$\Delta G_2 = E_{OH^*} + 0.5E_{H_2} - E_{H_2O^*} + (-eV) + F_2 \quad (8)$$
$$\Delta G_3 = E_{O^*} + 0.5E_{H_2} - E_{OH^*} + (-eV) + F_3 \quad (9)$$
$$\Delta G_4 = E_{OOH^*} + 0.5E_{H_2} - E_{O^*} - E_{H_2O} + (-eV) + F_4 \quad (10)$$
$$\Delta G_5 = 4.92 - \Delta G_1 - \Delta G_2 - \Delta G_3 - \Delta G_4 + F_5 \quad (11)$$

We define the quantity electrochemical overpotential as

$$\eta = \max\{\Delta G_2, \Delta G_3, \Delta G_4, \Delta G_5\} \quad (12)$$

For kMC simulations we need to define the forward and backward rate constants for each elementary step in the reaction. To obtain the rate constants as function of *V* for electrochemical steps, we adopt the following model[19]:

$$k_f^i(V) = A_f * \exp\left(-\frac{G_f^i(V)}{k_B T}\right) \quad (13a)$$
$$k_b^i(V) = A_b * \exp\left(-\frac{G_b^i(V)}{k_B T}\right) \quad (13b)$$

The subscript f denotes the forward reaction while the subscript b denotes the backward reaction. The quantities k, A, G, k_B, T denote the rate constant, pre-exponential factor, Gibbs free activation energy, Boltzmann constant and the temperature, respectively. The quantities $G_f^i(V)$ and $G_b^i(V)$ are given by[14b,19]:

$$G_f^i(V) = G_0^i + \beta \Delta G_i(V) \quad (14a)$$
$$G_b^i(V) = G_0^i - (1-\beta)\Delta G_i(V) \quad (14b)$$

In equations (14), G_0^i is the Gibbs free activation energy barrier for proton transfer when the forward and backward reactions are in equilibrium, i.e. $\Delta G_i(V) = 0$. The quantity β is the charge transfer coefficient which ensures that both the Gibbs free activation energies (G_f^i and G_b^i) are varied under the application of *V*. The theoretical value of β is 1.0 for semiconductors and 0.5 for metallic systems.[19] For example, Nørskov and co-workers found a transition coefficient of 0.5 for the ORR on Pt(111) surface using DFT.[14b] Since hematite is a semiconductor material, we have fixed $\beta = 1.0$ in our simulations which leads to $G_b^i(V) = G_0^i$ according to eq(14b). It should be noted here that our model mainly takes the TS barrier for proton transfer to be representative of the overall TS barrier for conversion of H_2O^* to OH^* (and the same holds for all the following steps). Such an approach is justified for metals where the transfer of electrons can be considered to be barrier less and such an approach has been applied in the literature for metallic systems.[14b,20] However, for semiconductor materials like hematite this might not be true. We note this limitation as a shortcoming of the way we currently model the TS barriers; this is a topic of ongoing investigation. Furthermore, we assume that the Gibbs free activation energies for all the electrochemical steps involving transfer of a proton from a surface bound O-X^* moiety (X = H_2, H etc.) is the same as that obtained for H_2O^*.[14c] Therefore,

$$G_b^i(V) = G_0^2 \quad (15)$$

for all electrochemical steps.

Computational Methods: This section describes the computational methods used in this manuscript. We have performed three types of calculations: (1) density functional theory (DFT) calculations (2) DFT based molecular dynamics (DFT-MD) simulations (3) kinetic Monte Carlo (kMC) calculations.

All DFT and DFT-MD simulations were performed using the ab-initio total-energy and molecular dynamics program VASP (Vienna Ab initio Simulation Package), version 5.4.1. [21]

DFT calculations: To treat the correlation of 3d electrons in Fe_2O_3, we chose the spin polarized DFT+U (U = 4.3 eV) formalism[15b]. The Perdew–Burke–Ernzerhof (PBE) XC functional[22] and the projected augmented wave (PAW) [23] potentials were used. We have used both a solid–gas model and an *implicit* solid-liquid model in our calculations. The *implicit* solid-liquid model describes the solvent effects using a continuum solvation model with the dielectric constant of water ($\epsilon = 78.4$) as implemented in VASPsol.[24] The geometries were fully optimized in vacuum and with VASPsol when incorporating solvent effects. The hematite slab consisted of a 2x2 supercell with 48 Fe and 72 O atoms. The unit cell was chosen from the hexagonal representation of hematite. Hematite was modelled as being in antiferromagnetic spin state (net zero spin for pristine surface).[15] Relevant input (INCAR) and output (CONTCAR) files are provided in the SI.

DFT-MD simulations: DFT-MD simulations incorporating the effect of temperature and explicit solvent molecules were used to compute the TS energy barrier for proton transfer from surface adsorbed species (e.g. H_2O^*) to a OH moiety in the solvent. We used a periodic simulation box with lattice vectors {(14.9829,0,0,),(-1.3002,10.9678,0),(0,0,24.0)} with the hematite, water and OH. The time-step in MD simulations was 0.5 fs. The overall system was charge-neutral. In the initial DFT-MD simulations of the hematite-water interface, we observed that the surface oxygens got immediately (< 100 fs) protonated. Therefore, the composition of the simulation box is as follows: 96 O atoms and 64 Fe atoms from Fe_2O_3, one OH moiety, 8 H moieties covering some of the surface oxygens, 66 water molecules.[25] Grimme's D3 method with Becke-Jonson damping (D3(BJ)) was adopted for the van der Waals correction applied via the IVDW = 12 and LVDWSCS = .True. flags as implemented in VASP.[26] We used BLYP XC functional for DFT-MD simulations because of better description of the structure and dynamics of water.[27] Projected augmented wave (PAW)[23] potentials were used. To generate a first estimate of the reaction free energy profile, we performed a coordinate drive calculation using the slow growth approach (SGA) as implemented in VASP. [28] Specifically, we simulated the transfer of a proton from a surface adsorbed water moiety (H_2O^*) to an OH moiety present in the second solvation layer (the first solvation layer is water that adsorbs directly at the surface). We chose the reaction coordinate (Q) to be the difference in distances of the proton being transferred to the adsorbed and solution phase oxygen moieties of the water and OH species (see *Figure* 1).[29]

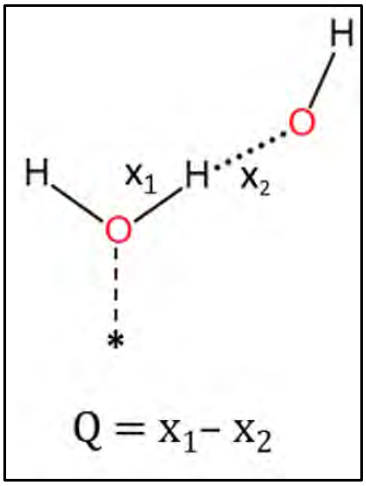

Figure 1. Reaction coordinate (Q) to simulate the transfer of proton from a H_2O^* species to an OH moiety in the second solvation layer.

Q was linearly varied from the reactant state ({H_2O^*, HO(aq)},Q = – 0.87 Å) to the product state ({OH*, H_2O(aq)},Q = +0.94 Å) by using the slow growth approach (SGA) with a transformation velocity of 5 x 10^{-4} Å/step. SGA simulations resulted in a rather noisy constrained force ($F(Q)$; force required to constrain Q) versus reaction coordinate (Q) profile (see Figure-SI-2). The force profile was further improved by averaging the constraining force ($< F(Q) >$) from longer constrained DFT-MD simulations which were run at 12 values of Q sampled from the trajectory obtained from the SGA calculations. Constrained DFT-MD simulations (~ 3-5 ps) were run for each of these points until the force on the constrained coordinates converged (force profiles are reported in the SI for each of these points). The average force was computed over the last 1.5 ps of DFT-MD simulations. Further computational details and relevant input/output files related to the DFT-MD simulations are reported in the SI.

kMC simulations: The kMC simulations were performed using the ZACROS suite of software.[30] The package employs the graph-theoretical kMC methodology coupled with cluster expansion Hamiltonians for the adlayer energetics. There are n_s =10^4 (100 x 100) square lattice sites modelled in the kMC simulations. The lateral interactions are not included in the present kMC simulations. Therefore, the number of species coordinated on neighbouring sites does not affect the simulation results. The pre-factors and rate constants used in kMC simulations with further relevant details are provided in the SI. Surface coverages at a given time t ($\theta_{X^*}(t)$, X = H_2O, OH, O, OOH) of various intermediates in the OER are computed as the number of surface species at any given time ($n_{X^*}(t)$) divided by the total number of lattice sites (n_s), that is

$$\theta_{X^*}(t) = \frac{n_{X^*}(t)}{n_s} \quad (16)$$

The initial state of the lattice is kept the same for all simulations at all values of applied potential.

Results and Discussion

DFT calculations: We first present the thermodynamic stabilities of various intermediates in the OER as computed using DFT calculations. The computed Gibbs free energy profile showing the relative stability of various intermediates in the mechanism of OER is presented in Figure 2 with and without implicit solvation.

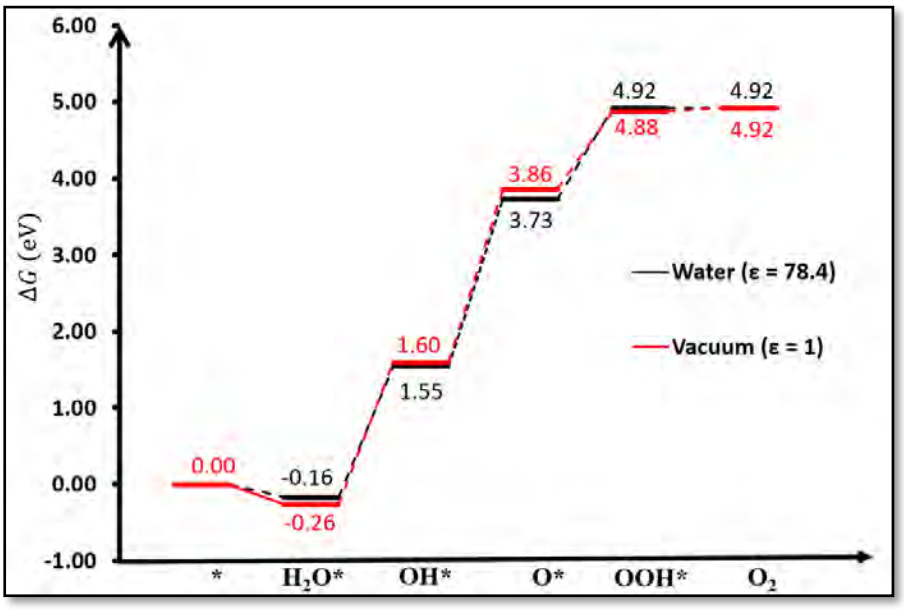

Figure 2. DFT computed Gibbs free energy (eq.(7) – eq(11)) profile for OER (eq.(1) – eq.(5)) over hematite 110 surfaces with (black) and without (red) implicit solvation corrections using VASPsol.

The adsorption of water on the hematite surface (eq(1)) is found to be exergonic both in vacuum and with solvation. This is in contrast to the calculations by Carter and co-workers[15b] who found endergonic adsorption of water on a 2x2 H covered (1/12 ML) 0001 surface of hematite in vacuum, and exergonic adsorption in the presence of an additional water molecule. This difference could stem from differences in the nature of the surface (110 vs 0001 and pristine vs H covered). The first electrochemical step (eq.(2), which converts H_2O^* to OH^*, is endergonic by 1.86 eV (vacuum) and 1.71 eV (water). The next step where OH^* converts to O^*, is endergonic by 2.26 eV (vacuum) and 2.18 eV (water), respectively. The next electrochemical steps (eq(4)-(5)) are relatively less endergonic in comparison to the first two electrochemical steps. Conversion of OOH^* species to O_2(g) completes the catalytic cycle releasing four equivalents each of H^+ and e^-. The conversion of OH^* to O^* is the largest step in the free energy profile and is therefore the potential (and overpotential defining) limiting step. The corresponding overpotential (eq.(12)) for OER is 0.95 eV (water; 1.03 eV in vacuum). [31] Carter and co-workers reported an overpotential of 0.77 eV for hematite 0001 surface.[15b] Note that we have considered atop binding mode for all the intermediates in OER and bridging binding modes have not been explored in this work. This could have resulted in relatively higher overpotentials. Moreover, Carter and co-workers used the electrochemical reaction potential of water as 1.11 V which is the DFT computed value with the entropy correction for water at 0.0035 bar. In contrast we have used the experimentally determined electrochemical potential of 1.23 V for the water splitting reaction. This difference (1.23 - 1.11 = 0.12 V) in electrochemical potentials also results in a relatively larger electrochemical overpotential in our model. Implicit solvent corrections confer an overall stability of 0.15 eV and 0.08 eV, respectively to the OH* and O* moieties compared to gas phase. Contrastingly the OOH* moiety is slightly (0.04 eV) destabilized in solvent compared to gas phase calculations. The overall impact of solvent corrections is minimal on the electrochemical overpotential (< 0.1 eV) and the relative stabilities of intermediates (< 0.2 eV).

DFT-MD simulations: The charge transfer reactions (2-5) involve the generation of an H^+ moiety at the solid-liquid interface which moves towards the liquid phase. Typically, such a transformation would involve an acceptor base moiety, such as OH or H_2O which would abstract the proton from a surface species (H_2O^*, OH^* etc.). We estimate TS_{H+} from H_2O^* to an acceptor base (OH (aq)) in the solvent phase.

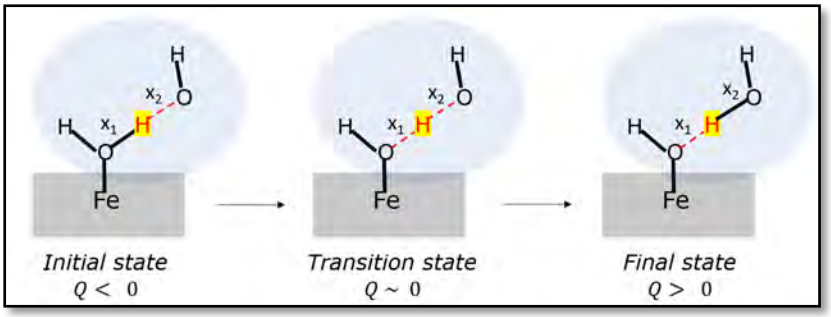

Figure 3: Schematic depiction of transfer of proton from H_2O^* species to an OH moiety in solvent with values of reaction coordinate (Q) for the proton transfer. The blue sphere represents the explicit solvent environment, the proton being transferred (H_t) is shown in red colored font with yellow highlight, the solid-state (hematite) is represented with a gray rectangle.

Figure 3 schematically shows the transfer of a proton from H_2O^* species to OH (aq). A negative Q value represents proximity of proton to be transferred (H_t) to the O moiety on H_2O^* which corresponds to the initial state (IS). At the TS, H_t is approximately midway between donor (from H_2O^*) and acceptor (OH(aq)) O atoms with a Q ~ 0. The final state when the proton is transferred to the OH(aq), has Q > 0 representing a higher proximity of the proton to the OH(aq). Figure 4 shows the snapshots of geometries from DFT-MD simulations close to the IS and the TS. In the IS, H_2O^* has an O-H_t bond length of ~1 Å. The OH(aq) is strongly hydrogen bonded to H_t at ~1.8 Å. This results in a Q value of ca. – 0.80 Å for the IS. In the TS, H_t is located approximately midway between the donor and acceptor O moieties (Q = 0.03 Å) (*Figure* 4 (right)).

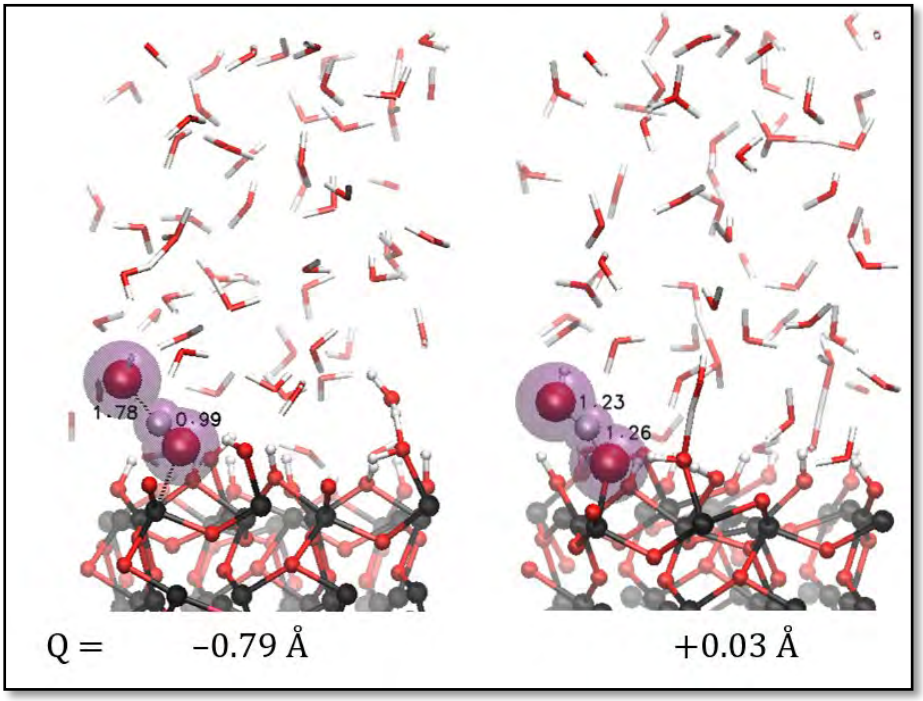

Figure 4. Snapshots of the hematite-water interface close to the IS (left) and TS (right) from DFT-MD simulations highlighting the transfer of proton to an acceptor OH moiety in the solvent at two values of Q. Color scheme: The atoms in the solvent are shown as sticks and those directly connected to the hematite are shown as spheres. Black spheres: Fe, red spheres: O. red sticks: O; white sticks: H. The O and OH species directly involved in the proton transfer reaction are shown as lager spheres and purple spheres are used to further highlight these atoms.

The average force profile ($< F(Q) >$) generated from DFT-MD simulations was integrated to obtain the corresponding free energy ($\Delta G\ (Q) = -\int_{Q=-0.87}^{Q=0.94} < F(Q) > dQ$) profile for the proton transfer reaction. The resulting Gibbs free energy profile for the proton transfer reaction from the H_2O^* moiety is shown in Figure 5.

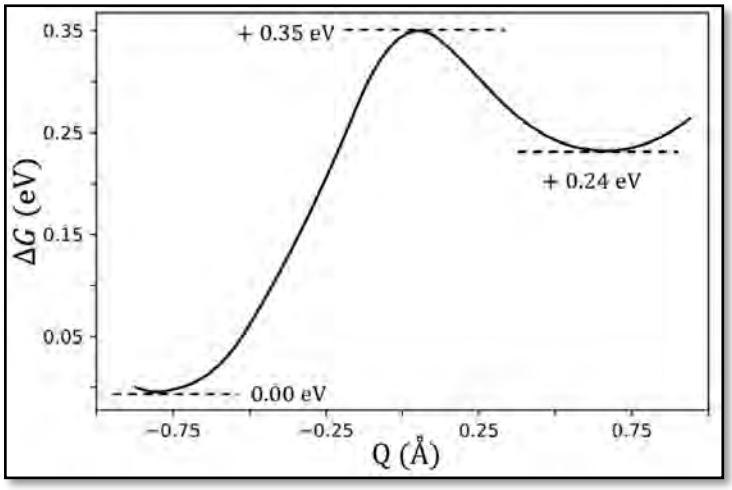

Figure 5. Computed Gibbs free energy profile for deprotonation of H_2O^* species using DFT-MD simulations. .

The proton transfer reaction is endergonic (+0.24 eV) . Such an endergonic proton transfer reaction indicates a decreased acidity ($pKa = pKa(H_2O) + \frac{\Delta G}{kT \cdot ln(10)} = 14 + \frac{0.24}{2.303 * 0.0257} \sim 18$) of water upon adsorption over the hematite surface.[32] This decreased acidity is indicative of charge transfer from H_2O^* to Fe (hematite), consistent with an exergonic formation of H_2O^* from DFT calculations. The Gibbs free energy barrier for TS_{H^+} from H_2O^* was obtained to be +0.35 eV ($G_f^2 = 0.35\ eV, G_b^2 = G_0^2 = 0.11\ eV$ (see $eq.(14)$). Oberhofer and co-workers computed TS_{H^+} from a surface adsorbed H_2O^* on rutile TiO_2 to be 0.2 eV with water as proton acceptor. Contrastingly, they found the deprotonation of water on rutile TiO2 to be exergonic by ~ - 0.5 eV.[29c] The higher TS_{H^+} for hematite probably results from a stronger binding of water and a relatively weaker binding of OH compared to TiO_2. We assume this free energy barrier of proton transfer from H_2O^* to be representative of the TS barrier for proton transfer during all charge-transfer reactions in OER (*vide supra*).[14c] A detailed investigation of the proton transfer reaction in other steps, such as conversion of OH^* to O^* will be part of a follow-up study.

kMC simulations: Having computed the thermodynamic stabilities and estimated TS_{H^+} for OER over hematite 110 surfaces, we can now define the rate constants for elementary steps (eq(1)-eq(5)) using the electrochemical model described by eq(7) – eq(15). As a first step, we combine the thermodynamic stabilities of intermediates in the OER with TS_{H^+} to make a reaction path model for OER over hematite (Figure 6).

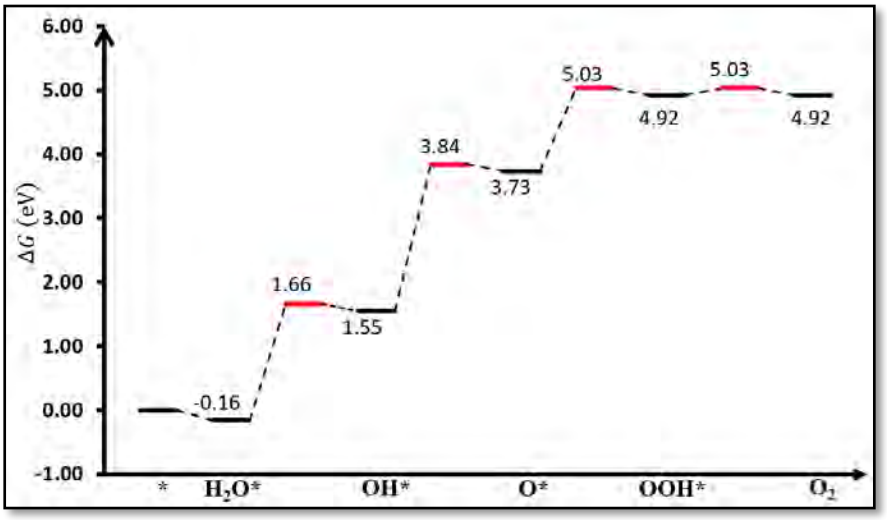

Figure 6. Reaction path model of OER combining the TS barriers obtained from DFT-MD simulations with relative thermodynamic stabilities of intermediates for charge transfer steps in the OER calculated using DFT. The transition states are shown as red lines.

The conversion of OH^* to O^* has the highest TS barrier in the OER. Using this reaction path model we can estimate the rate constants for the charge transfer reactions in OER (eq(2) – eq(5)) using eq(13) – eq(15) which, together

with the reaction mechanism (**M1/M2)** make the input for kMC simulations. We first describe the results of kMC simulations for mechanism **M1**.

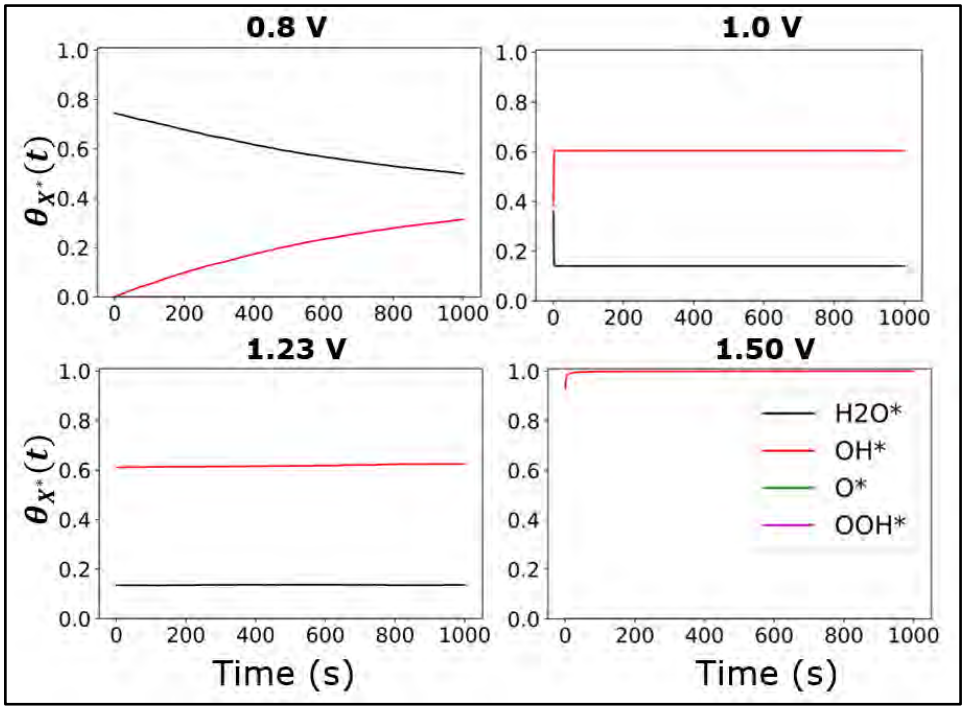

*Figure 7. Surface coverages of various intermediates (X^*, X = H_2O, OH, O, OOH) in OER at various values of V (indicated at top of each subplot) as a function of time for mechanism **M1** computed using kMC simulations. O^* and OOH^* species have negligible surface coverages. The coverages were calculated between t = 0.5 – 2000 s.*

Figure 7 shows $\theta_{X^*}(t)$ for mechanism **M1** as a function of time at various values of *V*. At *V* = 0.80 V, water dominates the surface. $\theta_{OH^*}(t)$ gradually builds up with time with a correlated decrease in $\theta_{H_2O^*}(t)$. At *V* = 1.0 V, $\theta_{OH^*}(t)$ exceeds $\theta_{H_2O^*}(t)$. At *V* = 1.23 V, which is the equilibrium potential for OER, $\theta_{H_2O^*}(t)$drops below 20%. At even higher potentials (*V* = 1.50 V) $\theta_{OH^*}(t)$ further increases and $\theta_{H_2O^*}(t)$ becomes negligible. $\theta_{OH^*}(t)$ and $\theta_{H_2O^*}(t)$ are approximately constant beyond 0.80 V indicating a build-up of OH coverage at the surface. The time-dependent surface coverages calculated at various values of *V* give important insight into the rate of OER at hematite. According to the reaction path model (Figure 6) the conversion of OH* to O^* is potential limiting and has the highest TS barrier. The surface coverage plots reveal that the coverage of OH species builds up on the surface indicating that its conversion is also the rate limiting step in OER.

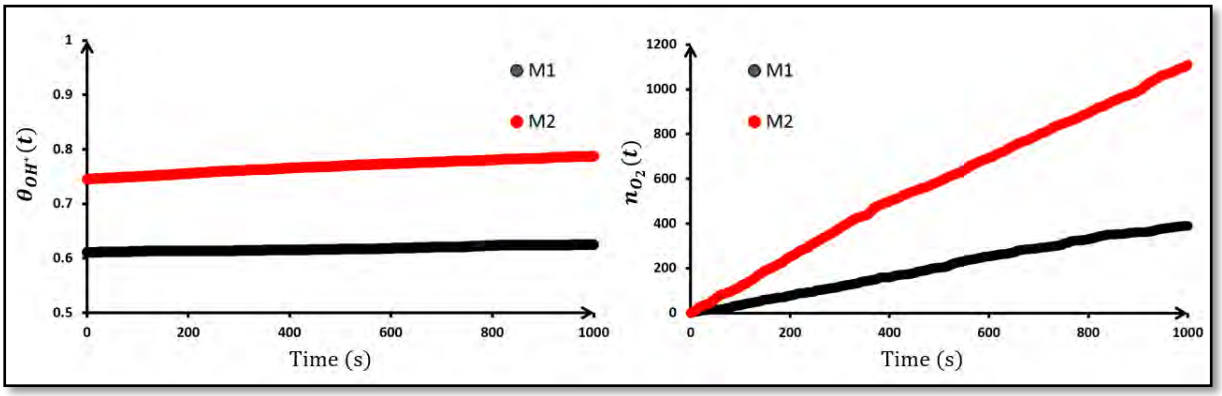

Figure 8. (left) Surface coverage of OH^* ($\theta_{OH^*}(t)$) and (right) number of O_2 molecules ($n_{O_2}(t)$) formed as a function time at V = 1.23 V vs CHE. Black and red lines denote the M1 and M2 mechanism, respectively.

Next, we performed kMC simulations for mechanism **M2** to compare it with **M1** and quantitatively investigate the impact of explicitly modelling eq(1) in OER. In mechanism **M2**, the Gibbs free energy for formation of OH^* is 1.55 eV (water) in contrast to a Gibbs free energy of 1.71 eV (water) in **M1**. This difference in relative stabilities (1.71 – 1.55 = 0.16 eV) arises due to exergonic adsorption (-0.16 eV) of water over hematite. Figure 8 (left) shows $\theta_{OH^*}(t)$ at 1.23 V for **M1** and **M2**. **M2** features a higher $\theta_{OH^*}(t)$ early on and it slowly grows to almost 80% at t = 1000s. In contrast, **M1** features an approximately constant $\theta_{OH^*}(t)$ ~60%. The evolution of O_2 (Figure 8 (right)) increases linearly in both **M1** and **M2**. The time-dependent surface coverages and curves for oxygen evolution curves for various applied potentials for mechanisms **M1** and **M2** are presented in the SI. $\theta_{OOH^*}(t)$and $\theta_{O^*}(t)$ are negligible for both **M1** and **M2** while H_2O (in case of **M1**) and OH dominate the surface. At higher potentials (V > 1.30 V), the surface is mainly covered with OH moiety which is consistent with its conversion being the rate limiting step (*vide supra*). We applied our multiscale model to demonstrate the importance of explicitly modelling the adsorption of water (mechanism **M1**) from a kinetics perspective which is often omitted (mechanism **M2**) in DFT based mechanistic studies.

Adsorption of water on the hematite surface has recently been proposed to have a possible impact on the electrochemical overpotential on metal oxides based on spectroscopic measurements.[16] kMC simulations of **M1** and **M2** showed an excess $\theta_{OH^*}(t)$ by 20% in the mechanism **M2** at 1.23 V. This excess $\theta_{OH^*}(t)$ in **M2** is likely to be an overestimate resulting from omission of thermochemical adsorption of water. Consequently, mechanism **M2** also indicated a much higher rate of oxygen evolution which is also likely to be overestimated. However, at higher potential (V > 1.30 V) the difference in surface coverage of OH* between M1 and M2 becomes insignificant (refer to Figure-SI-3). Since formation of OH* is not the rate limiting step, the behavior of the system is dominated by the rate limiting step at higher potential (V > 1.30 V). However, divergent surface coverages at intermediate potentials (V < 1.30 V) can be of mechanistic significance if adsorbate-adsorbate interactions are included in the model. Adsorbate-adsorbate interactions can influence the relative stabilities of intermediates in OER and also influence the rate constants. It is therefore important to explicitly model the interaction of solvent with the electrode. In OER systems where formation of OH* is the potential limiting step or its energy is comparable to the potential limiting step, explicit modelling of adsorption of water and thereby solvent effects in the mechanism become even more important. In such a scenario the adsorption energy of water can possibly influence the overpotential in the system and impact surface coverages/OER kinetics also at larger V (V > 1.30 V).

Summary, Conclusions and Outlook

We present a novel multiscale modelling method to investigate the mechanism of OER by coupling and linking DFT, DFT-MD and kMC simulations. The 110 surface of hematite was used as model system in this study. DFT calculations indicated that the formation O^* species is the potential limiting step in the OER over hematite. DFT calculations further revealed that solvent effects within a continuum solvation model had minimal impact (< 0.2 eV) on the relative stability of intermediates in the OER over hematite. DFT-MD simulations uncovered that the acidity of water reduces upon adsorption over the hematite surface which results in an endergonic (+0.24 eV) proton transfer reaction with a transition state barrier of 0.35 eV. This transition state barrier was assumed to represent the transition state barrier for all the proton transfer steps in the OER mechanism. The thermodynamic stabilities and transition state barriers for various steps in the OER computed from DFT and DFT-MD simulations respectively were combined to create a reaction path model for OER at the hematite-water interface. Rate constants for elementary steps in OER were estimated using this reaction path model and along with the reaction mechanism were used as input for kMC simulations. The multiscale model was used to elucidate time and voltage dependent surface coverages of various intermediates in OER at the hematite-water interface. Furthermore the multiscale model was used to investigate the impact of modelling the interaction of water with the hematite surface via explicit chemisorption. The impact of modelling explicit adsorption of water in the reaction mechanism, and particular cases where it can be of mechanistic importance were discussed.

To the best of our knowledge a multiscale model of OER coupling DFT, DFT-MD and kMC has not been reported in the literature yet. Our multiscale model enables simulation of time and applied bias potential dependent surface coverages of various intermediates during the OER. This is data which is experimentally not available, but very useful in order to design tailored electrodes. The multiscale model enables us to compare two different mechanisms of OER and allows us to examine the impact of explicitly modelling the interaction of water with the electrode surface. We have shown how one can connect DFT, DFT-MD and kMC calculations within a multiscale modelling framework to simulate electrochemical data which has direct experimental relevance. The next step is to further refine the multiscale model by further improving the mechanistic picture and the electrochemical model. From a mechanistic perspective, several research questions can be investigated to improve the multiscale model. For example, the thermodynamic stabilities of various OER intermediates need to be examined with explicit solvation, different binding modes (atop, bridging, co-adsorption of intermediates) of intermediates need to be examined. DFT-MD simulations for proton transfer reactions should also be performed with H_2O as acceptor base

to realistically capture the kinetics of the system at low pH. Moreover, one needs to compute the transition state barrier for proton transfer during formation of O^*, OOH^* and O_2. With regards to the examination of solvent effects, it would be desirable to compute the transition state barriers for the proton transfer reaction using static DFT calculations with a cluster representation of the solvent with increasing number of solvent molecules to quantify the impact of solvation and flexibility of the solvent environment on the barrier for proton transfer reactions. From an electrochemical modelling perspective, potential dependent rate constants are currently computed using the transition state barrier for proton transfer. These rate equations should be improved with a more realistic modelling which also includes the rate of transfer of e^- explicitly. The multiscale modelling approach in this paper relies on coupling and linking of DFT, DFT-MD and kMC simulations within an electrochemical model defined by eq(7) – eq(15). Since we have performed DFT and DFT-MD simulations at different levels of theory our multiscale model should be tested with a sensitivity analysis based on propagation of errors from various source related to the model itself and the computational method (error from DFT and DFT-MD). Finally the multiscale model needs to be validated against experimental data such as by simulating the onset potential and the polarization curve for OER. The multiscale model presented in this work will pave the way for obtaining valuable mechanistic insights into OER under operando conditions for various photoanode materials.

Conflict of interest

There are no conflicts of interest to declare

Acknowledgements

V.S., A.B.H. and T.J.H.V. acknowledge financial support from MERA.NET (project “MuMo4PEC” with project number MERA.NET 4089). A.B.H. acknowledge the financial support from NWO (FOM program nr. 147 “CO2 neutral fuels”). This work was carried out on the Dutch national e-infrastructure with the support of SURF Cooperative. V.S. and A.B.H. thank Dr. B. Szyja, Wroclaw University, Poland, for additional computing time as well as fruitful discussions. Mr. K. George (DIFFER), Mrs. Q. Liang (DIFFER), Dr. A. Khetan (DIFFER) and Mr. N. Govindarajan (University of Amsterdam) are acknowledged for stimulating discussions. The authors thank Dr. X. Zhang (DIFFER) for support in DFT and kMC simulations. T.J.H.V acknowledges NWO-CW for a VICI grant.

Notes and References

[1] a) B. M. H. Weninger and F. M. Mulder, *ACS Energy Lett.*, 2019, **4**, 567−571. b) J. Gong, C. Li, M. R. Wasielewski, *Chem. Soc. Rev.*, 2019, **48**, 1862. c) Research needs towards sustainable production of fuels and chemicals, Executive ed. J. K. Nørskov, https://www.energy-x.eu/wp-content/uploads/2019/10/Energy-X-Research-needs-report.pdf . Accessed: 04/12/2019.
[2] X. Zhang, A. Bieberle-Hütter, *ChemSusChem*, 2016, **9,** 1223.
[3] B. Iandolo, B. Wickman, I. Zori and A. Hellman, *J. Mater. Chem. A*, 2015, **3**, 16896.
[4] a) R. F. G. Gardner, F. Sweett and D. W. Tanner, *J. Phys. Chem. Solids*, 1963, **24**, 1175. b) S. M. Sze and K. K. Ng, *Physics of Semiconductor Devices*, 2006, **3rd edn**., Wiley.
[5] a) A. Kay, I. Cesar and M. Grätzel, *J. Am. Chem. Soc.*, 2006, **128**, 15714. b) P. Zhang, A. Kleiman-Shwarsctein, Y.-S. Hu, J. Lefton, S. Sharma, A. J. Forman and E. McFarland, *Energy Environ. Sci.*, 2011, **4**, 1020. c) S. C. Warren, K. Vöıtchovsky, H. Dotan, C. M. Leroy, M. Cornuz, F. Stellacci, C. Hèbert, A. Rothschild and M. Grätzel, *Nat. Mater.*, 2013, **12**, 842.
[6] a) A. G. Tamirat, J. Rick, A. A. Dubale, W.-N. Su, and B.-J. Hwang, *Nanoscale Horiz.,* 2016, **1**, 243. b) C. Ding, J. Shi, Z. Wang, and C. Li, *ACS Catal.*, 2017, **7**, 675. c) F. Malara, A. Minguzzi, M. Marelli, S. Morandi, R. Psaro, V. Dal Santo and A. Naldoni, *ACS Catal.*, 2015, **5**, 5292. d) K. George, X. Zhang and A. Bieberle-Hütter, *J. Chem. Phys.*, 2019, **150**, 041729.
[7] a) X. Zhao, J. Feng, S. Chen, Y. Huang, T. C. Sum and Z. Chen, *Phys. Chem. Chem. Phys.*, 2017, **19**, 1074. b) X. Zhang, P. Klaver, R. Santen, M.C.M. Sanden and A. Bieberle-Hütter, *J. Phys. Chem. C*, 2016, **120**, 18201.
[8] a) O. Zandi, T. W. Hamann, *Nature Chemistry*, 2016, **8**, 2557. b) F. L. Formal, E. Pastor, S. D. Tilley, C. A. Mesa, S. R. Pendlebury, M. Grätzel and J. R. Durrant, *J. Am. Chem. Soc.*, 2015, **137**, 6629.
[9] K. George, M. van Berkel, X. Zhang, R. Sinha and A. Bieberle-Hütter, *J. Phys. Chem. C*, 2019, **123**, 9981.
[10] a) J.A. Gauthier, C. F. Dickens, L. D. Chen, A. F. Doyle and J. K. Nørskov, *J. Phys. Chem. C*, 2017, **121**, 11455. b) J. K. Nørskov, J. Rossmeisl, A. Logadottir, L. Lindqvist, J. R. Kitchin, T. Bligaard and H. Jónsson, *J. Phys. Chem. B*, 2004, **108**, 17886. c) V. Tripkovic, E. Skulason, S. Siahrostami, J. K. Nørskov, J. Rossmeisl, *Electrochim. Acta*, 2010, **55**, 7975. d) G. S. Karlberg, *Phys. Rev. B*, 2006, **74**, 153414. e) J. Rossmeisl, J. Greeley, G. S. Karlberg, Fuel Cell Catalysis: A Surface Science Approach; John Wiley & Sons, Inc.: Hoboken, NJ, 2009. f) F. Calle-Vallejo, J. I. Martínez, J. Rossmeisl, *Phys. Chem. Chem. Phys.*, 2011, **13**, 15639. g) S. Liu, M. G. White, P. Liu, *J. Phys. Chem. C*, 2016, **12**0, 15288. h) L. G. V. Briquet, M. Sarwar, J. Mugo, G. Jones, F. Calle-Vallejo, *ChemCatChem*, 2017, **9**, 1261. i) L. P.Granda-Marulanda, S. Builes, M. T. M. Koper, F. Calle-Vallejo, *Chem. Phys. Chem.*, 2019, **20**, 2968.
[11] a) O. R. Gittus, G. F. Rudorff, K. M. Rosso, J. Blumberger, *Phys. Chem. Lett.*, 2018, **9**, 5574. b) G. F. Rudorff, R. Jakobson, K. M. Rosso, J. Blumberger, *J. Phys. Chem. Lett.*, 2016, **7**, 1155. c) G. F. Rudorff, R. Jakobson, K. M. Rosso, J. Blumberger, *J. Phys.: Condens. Matter*, 2016, **28**, 394001. d) M. E. McBriarty, G. F. Rudorff, G. F. von Rudorff, J. E. Stubbs, P. J. Eng, J. Blumberger, K. M. Rosso, *J. Am. Chem. Soc.*, 2017, **139**, 2581.
[12] L. Schöttner, R. Overcharneko, A. Nefedov, E. Voloshina, Y. Wang, J. Sauer, C. Wöll, *J. Phys. Chem. C*, 2019, **123**, 8324.

[13] K. Mathew, R. Sundararaman, K. Letchworth-Weaver, T. A. Arias, R. G. Hennig, *J. Chem. Phys.*, 2014, **140**, 084106. b) K. Mathew, R. G. Hennig, R. G. ArXiv, 2016, https://arxiv.org/abs/1601.03346.
[14] a) M. J. Janik, C. D. Taylor, M. Neurock, *Journal of The Electrochemical Society*, 2009, **156,** B126. b) V. Tripkovi`c, E. Skúlason, S. Siahrostami, J. K. Nørskov, J. Rossmeisel, Electrochimica Acta 2010, **55**, 7975.
[15] a) R. B. Wang and A. Hellman, *J. Phys. Chem. C*, 2019, **123**, 2820. b) P. Liao, J. A. Keith, and E. A. Carter, *J. Am. Chem. Soc.*, 2012, **134**, 13296. c) C. F. Dickens, C. Kirk and J. K. Nørskov, *J. Phys. Chem. C*, 2019, **123**, 18960.
[16] Z. Jakub et al., *ACS Energy Lett.*, 2019, **4**, 390.
[17] J. Rossmeisl, Z. W. Qu, H. Zhu, G. J. Kroes and J. K. Nørskov, *J. Electroanal. Chem.*, 2007, **607**, 83.
[18] J. K. Nørskov, J. Rossmeisl, A. Logadottir, L. Lindqvist, J. R. Kitchin, T. Bligaard and H. Jonsson, *J. Phys. Chem. B*, 2004, **108**,17886.
[19] See chapter 7 in Semiconductor Electrochemistry, Ed. by Rüdiger Memming, 2nd edition, Wiley-Vch.
[20] H. A. Hansen, V. Viswanathan and J. K. Nørskov, *J. Phys. Chem. C*, 2014, **118**, 6706.
[21] a) https://www.vasp.at/. b) G. Kresse and D. Joubert, *Phys. Rev. B: Condens. Matter Mater. Phys.*, 1999, **59**, 1758. c) O. Bengone, M. Alouani, P. Blöchl and J. Hugel, *Phys. Rev. B: Condens. Matter Mater. Phys.*, 2000, **62**, 16392. d) G. Kresse and J. Furthmüller, *Comput. Mater. Sci.*, 1996, **6**, 15. e) G. Kresse and J. Furthmüller, *Phys. Rev. B: Condens. Matter Mater. Phys.*, 1996, **54**, 11169.
[22] J. P. Perdew, K. Burke and M. Ernzerhof, *Phys. Rev. Lett.*, 1996, **77**, 3865.
[23] P. E. Blöchl, *Phys. Rev. B: Condens. Matter Mater. Phys.*, 1994, **50**, 17953.
[24] http://vaspsol.mse.ufl.edu/
[25] Note that the size of hematite supercell used in DFT-MD simulations is larger (64Fe, 96 O) than that used for DFT calculations because of different representations of the unit cell (rhombohedral for DFT-MD and hexagonal for DFT). Since periodic boundary conditions are applied (also see snapshots of the molecular model of hematite with PBC for DFT and DFT-MD simulations in the SI) we expect this difference in size of the supercell to not add any significant difference in our simulations.
[26] S. Grimme, J. Antony, S. Ehrlich, H. Krieg, *J. Chem. Phys.*, 2010, **132,** 154104 b) S. Grimme, S. Ehrlich, L. Goerigk, *J. Comput. Chem.*, 2011, **32**, 1456.
[27] a) A. D. Becke, *Phys. Rev. A*, 1988, **38**, 3098. b) C. Lee, W. Yang and R.G. Parr, *Phys. Rev. B*, 1988, **37**, 785. c) B.G. Johnson, P.M.W. Gill and J.A. Pople, *J. Chem. Phys.*, 1993, **98**, 5612. d) T.V. Russo, R.L. Martin and P.J. Hay, *J. Chem. Phys.*, 1994, **101**, 7729. e) M. Sprik, J. Hutter, M. Parrinello. *J. Chem. Phys.*, 1996, **105**, 1142.
[28] a) T. K. Woo, P. M. Margl, P. E. Blöchl and T. Ziegler, *J. Phys. Chem. B*, 1997, **101**, 7877. b) C. Jarzynski, *Phys. Rev. Lett.*, 1997, **78**, 2690. c) C. Oberhofer, C. Dellago and P. L. Geissler, *J. Phys. Chem. B*, 2005, **109**, 6902.
[29] For an accurate calculations of the transition state barrier for proton transfer one needs a topologically invariant reaction coordinate. However, such calculations for hematite-water interface would be non-trivial and outside the scope of our current research. We note this as a limitation of our study. Please see a) L. Mones and C. Csànyi, *J. Phys. Chem. B*, 2012, **116**, 14876. b) L. Mones, P. Kulhànek, I. Simon, A. Laio and M. Fuxreiter, *J. Phys. Chem. B*, 2009, **113**, 7867. c) T. Stecher, K. Reuter and H. Oberhofer, *Phys. Rev. Lett.*, 2016, **117**, 276001.
[30] a) W. Nielsen, M. d'Avezac, J. Hetherington, M. Stamatakis, *J. Chem. Phys.*, 2013, **139**, 224706. b) M. Stamatakis and D. G. Vlachos, *Journal of Chemical Physics*, 2011, **134**, 214115.
[31] Note that a previous work from our (X. Zhang, C. Cao and A. Bieberle-Hütter, *J. Phys. Chem. C*, 2016, **120**, 28694) reported lower overpotential of 0.78 eV for OER over 110 surface of hematite. However those calculations were assumed a ferromagnetic spin state of hematite which may have resulted in a low overpotential.
[32] We would like to emphasize that we only intend to make a rough estimate of the pK_a here. An accurate calculation of pK_a should be done with a more sophisticated technique such as thermodynamic integration introduced by Sprik and co-workers, see: a) J. Cheng, M. Sulpizi and M. Sprik, *J. Chem. Phys.*, 2009, **131**, 154504. b) M. Sulpizi and M. Sprik, *J. Phys.: Condens. Matter*, 2010, **22**, 284116. c) J. Cheng, X. Liu, J. VandeVondele, M. Sulpizi and M. Sprik, *Acc. Chem. Res.*, 2014, **47**, 3522.

Supporting Information

A Multiscale Modelling Approach to Elucidate the Mechanism of the Oxygen Evolution Reaction at the Hematite-Water Interface

V. Sinha[*1,2], D. Sun[3], E. J. Meijer[3], T. J. H. Vlugt[*2], A. Bieberle-Hütter[*1]

[1] Electrochemical Materials and Interfaces, Dutch Institute for Fundamental Energy Research (DIFFER), de Zaale 20, 5612 AJ, Eindhoven, The Netherlands

[2] Process and Energy Department, Faculty of Mechanical, Maritime and Materials Engineering, Delft University of Technology, Leeghwaterstraat 39, 2628CB, Delft, The Netherlands

[3] Amsterdam Center for Multiscale Modelling, HIMS, University of Amsterdam, Amsterdam, The Netherlands.

* corresponding authors: V.Sinha@differ.nl, T.J.H.Vlugt@tudelft.nl, A.Bieberle@differ.nl

Force profile from constrained DFT-MD

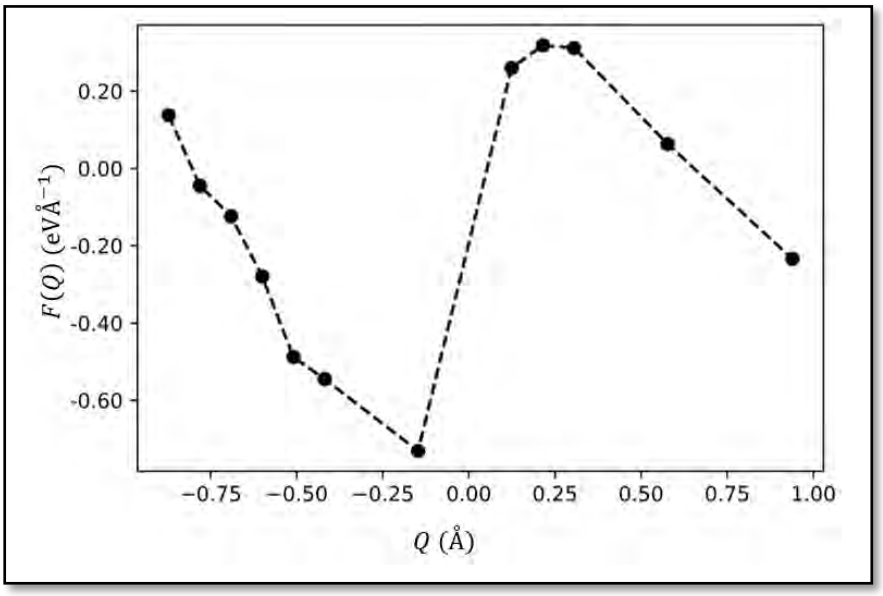

Figure-SI- 1. Force profile obtained from DFT-MD simulations. Each point was run for 3-5 ps and the resulting profile was integrated to construct the Gibbs free energy profile reported in the main text (Figure 5).

Force and Gibbs free energy profiles from steered MD using slow growth approach

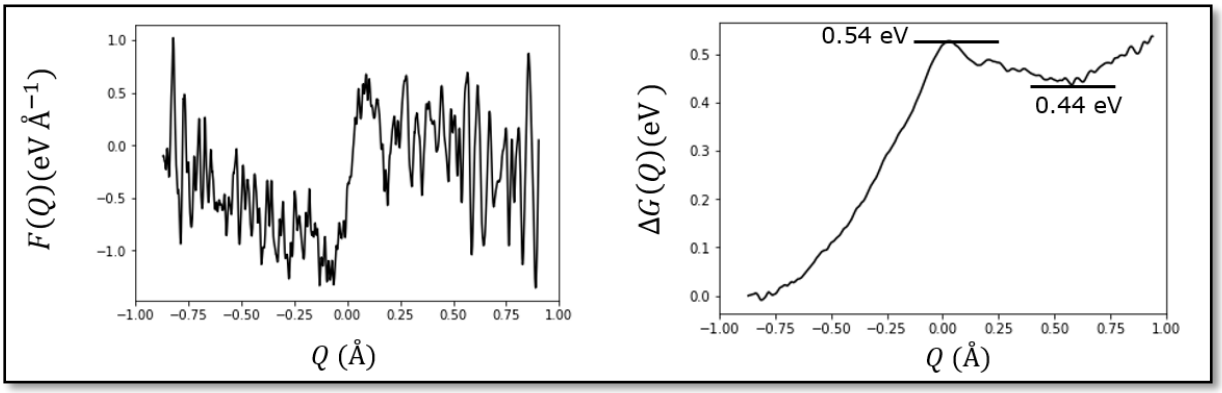

Figure-SI- 2. (left) force profile from slow growth approach simulations to simulate the proton transfer reaction. (right) Gibbs free energy profile for the proton transfer reaction obtained by integrating the force profile.

Comparison of OH coverage for mechanisms M1 and M2

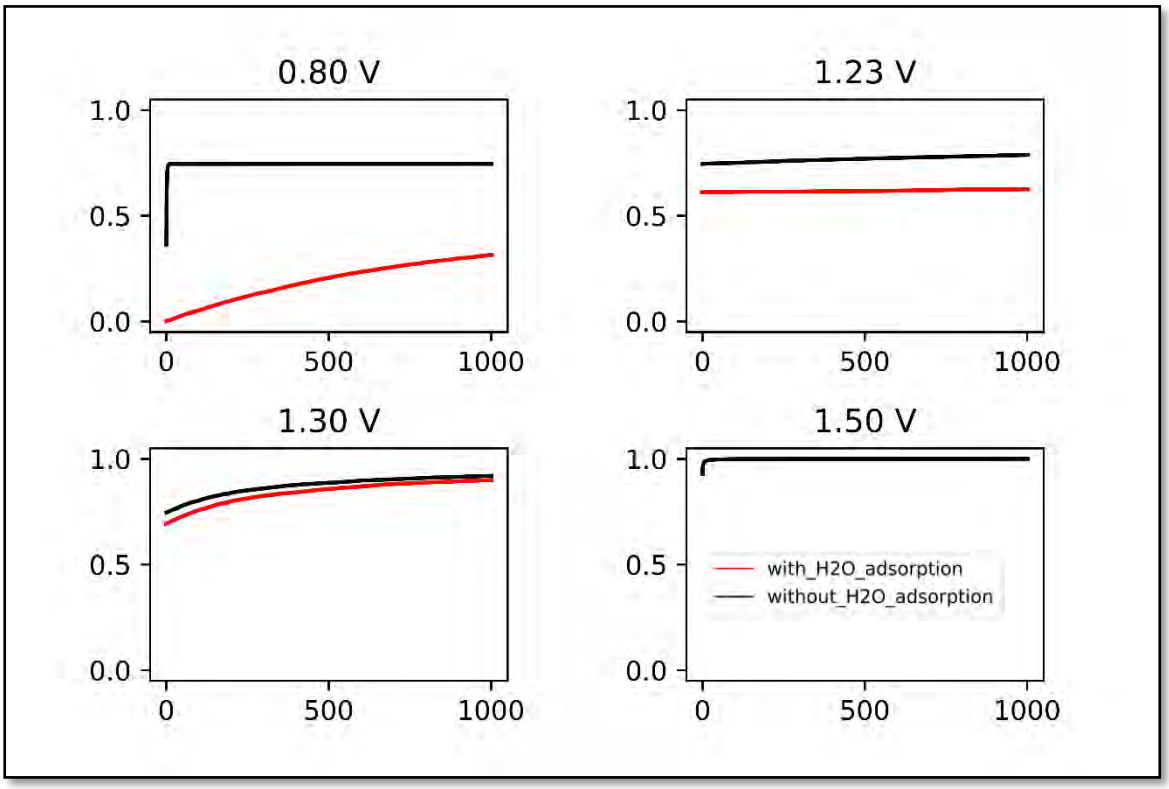

Figure-SI- 3. Comparison of surface coverage of OH (y-axis) as a function of time (x-axis) for various values of the applied bias for mechanisms M1 (red, with H_2O adsorption) and M2 (black, without H_2O adsorption).

Comparison of O_2 evolution for mechanisms M1 and M2

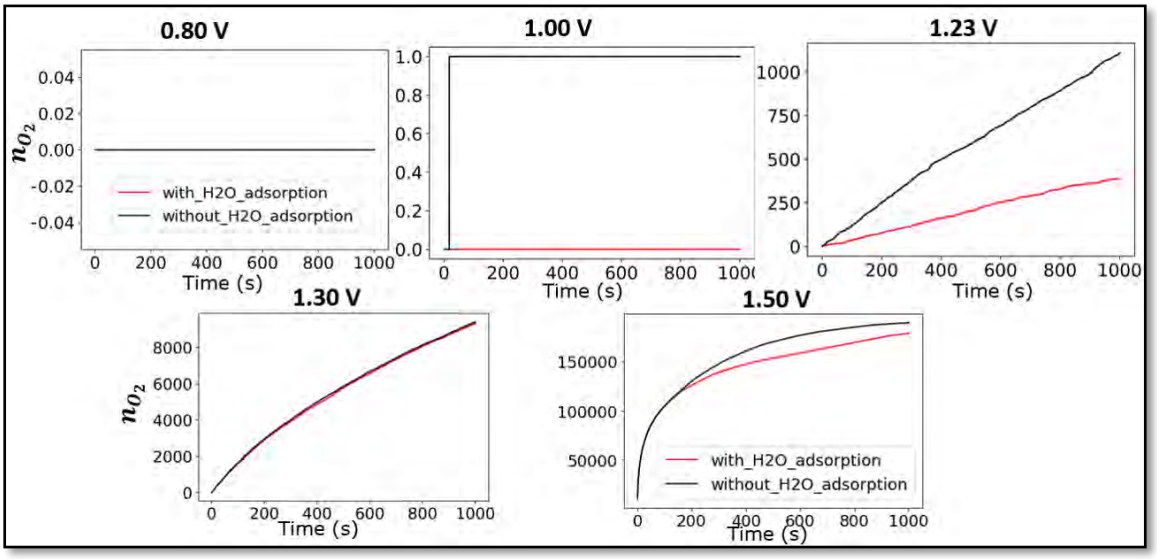

Figure-SI- 4. Comparison of O_2 evolution as a function of time for various values of the applied bias for mechanisms M1 (red, with H2O adsorption) and M2 (black, without H2O adsorption).

Rate constants for kMC

Rate of individual steps in kMC were determined by eq(13) as described in the main text

$$k_f^i = A_f * \exp\left(-\frac{G_f^i}{k_B T}\right) \qquad (13a)$$

$$k_b^i = A_b * \exp\left(-\frac{G_b^i}{k_B T}\right) \qquad (13b)$$

The adsorption of water was modelled as follows:

Forward reaction, adsorption: $A_f = 10^5\ s^{-1}$ and $G_f = 0.00$ eV

Backward reaction, desoprtion: $A_b = 1$ and $G_b = 0.2$ eV

For modelling the adsorption/desoprtion of water the parameters $\{A_f, A_b, G_f, G_b\}$ were chosen to ensure that most of the wall-time is kMC simulations is not used in simulating fast reversible process of adsorption of water. For rest of the steps which are all electrochemical in nature we used the same pre-factors ($A_f = A_b = 10^{14}\ s^{-1}$) for the forward and the backward reaction.

Table-SI- 1. TS barriers for forward and backward reactions in mechanism M1 for selected values of V. Potential dependent rate constants can be evaluated from this data using eq(13)

V	$TS_{\{H_2O\to OH\}}$	$TS_{\{OH\to H_2O\}}$	$TS_{\{OH\to O\}}$	$TS_{\{O\to OH\}}$	$TS_{\{O\to OOH\}}$	$TS_{\{OOH\to O\}}$	$TS_{\{O_2\to OOH\}}$	$TS_{\{OOH\to O_2\}}$
0.0	1.82	0.11	2.29	0.11	1.30	0.11	0.11	0.11
0.8	1.02	0.11	1.49	0.11	0.5	0.11	0.00	0.11
1.0	0.82	0.11	1.29	0.11	0.30	0.11	0.00	0.11
1.23	0.59	0.11	1.06	0.11	0.07	0.11	0.00	0.11
1.30	0.52	0.11	0.99	0.11	0.00	0.11	0.00	0.11
1.50	0.32	0.11	0.79	0.11	0.00	0.11	0.00	0.11

Representative INCAR files

Geometry Optimizations

SYSTEM = Fe2O3 ionic relaxation
ICHARG = 1 initial charge density option
ISTART = 1 initial wavefunctions option
PREC = Medium precision of calculation
NELM = 60 max number of electronic steps
NELMIN = 2 min number of electronic steps
EDIFF = 1E-04 energy stopping criterion for electronic iterations
EDIFFG = -1E-02 force stopping criterion for geometric
LREAL = A real-space projection
ALGO=Very Fast choose algorithm
NSIM=4 parallelization option
ISPIN=2 spin-polarization option
ISYM = 0 turns symmetry calculation on or off
ISIF = 2 geometrical relaxation mode
NSW = 300 max number of geometry steps
IBRION = 2 ionic relaxation method
POTIM = .07 time step for geometrical optimization
ISMEAR = 0 smearing method
SIGMA = .100 broadening in eV

```
   ENCUT = 700
MAGMOM = 72*0 24*-4 24*4    #corresponding to 72 O and 48 Fe
RWIGS = 0.8 1.2
LDAU = .TRUE.
LDAUTYPE = 2
LDAUL = -1 2
LDAUU = 0.0 4.30
LDAUJ = 0.00 0.00
LDAUPRINT = 2
LWAVE = F
LSOL = T
```

DFT-MD simulations

```
  SYSTEM   =  Fe2O3
# Start parameter for this run:
!  NWRITE =      2
   PREC   =    low
   ISTART =      1
   ICHARG =      1
   ISPIN  =      2
!  NBANDS =     120
   MAGMOM =     32*-4.0  32*4.0   96*0.0   208*0.0
!  LNONCOLLINEAR =  F
!  LSORBIT=      F
!  INIWAV =      1
!  LASPH  =      F
!  METAGGA=      F
# Electronic Relaxation 1
   ENCUT   =  500.0 eV
   ENAUG   =  600.0 eV
   EDIFF   =  1E-06
   LREAL   =  Auto
!  VOSKOWN =  1
!  NELM    = 40
   NELM    = 40;   NELMIN=  8
!  ENINI   =  200.0
!  LCOMPAT =  F
!  LREAL_COMPAT= F
!  GGA_COMPAT  = T
!  LMAXPAW     = -100
!  LMAXMIX     =    2
!  ROPT        =    0.00000
# Electronic relaxation 2 (details)
   ALGO   =   Very Fast
!  IALGO  =    38
!  LDIAG  =     T
!  IMIX   =     4
!  AMIX   =   0.80;   BMIX     =  1.00
!  AMIX_MAG =   3.20;   BMIX_MAG =  1.00
!  AMIN   =   0.10
!  WC     =   100.;   INIMIX=   1;  MIXPRE=   1
# Ionic relaxation
```

```
!  EDIFFG  =
!  ISIF    =
   NSW     =   1000
   IBRION  =     0
!  NBLOCK  =     1;   KBLOCK =     1
!  NFREE   =     0
!  IWAVPR  =    10
   ISYM    =     0
!  LCORR   =     T
   POTIM   =  0.50
!  TEIN    =  350
   TEBEG   =  350.0;   TEEND  =  350.0
   SMASS   =  0
!  NPACO   =   256;   APACO  = 16.0
!  PSTRESS =   0.0
!  MDALGO  =   11

# DOS related values:
   ISMEAR  =     0;   SIGMA  =   0.05
!  EMIN    =  10.00;   EMAX   =-10.00
# Write flags
   LWAVE   =     F
   LCHARG  =     F
   LVTOT   =     F
!  LELF    =
!  LORBIT  =
#  Atomic Wigner-Seitz radii
!  RWIGS   =  -1.00
!  NELECT  =      1.0000
!  NUPDOWN =     -1.0000
#  Mass of Ions in am
  #Fe   Fe   O    O        O    H
   POMASS  =   55.8 55.8 16.0 16.0 16.0 2.0  # Deuterium mass for H
# BLYP
   GGA   = B5
   ALDAX = 1.00
   AGGAX = 1.00
   AGGAC = 1.00
   ALDAC = 0.00
# vdW correction
  IVDW    = 12
  LVDWSCS = .TRUE.
# meta dynamics
   MDALGO     =  2
!  HILLS_H    =  0.1E-2
!  HILLS_W    =
!  HILLS_BIN  =  50
   LBLUEOUT   =  .TRUE.
!   INCREM    =  0.0005
NPAR = 16
```

The CONTCAR files from geometry optimizations with and without VASPsol, and the force profiles from constrained DFT-MD simulations are provided separately as a .zip file.

Molecular models of hematite in DFT and DFT-MD simulations

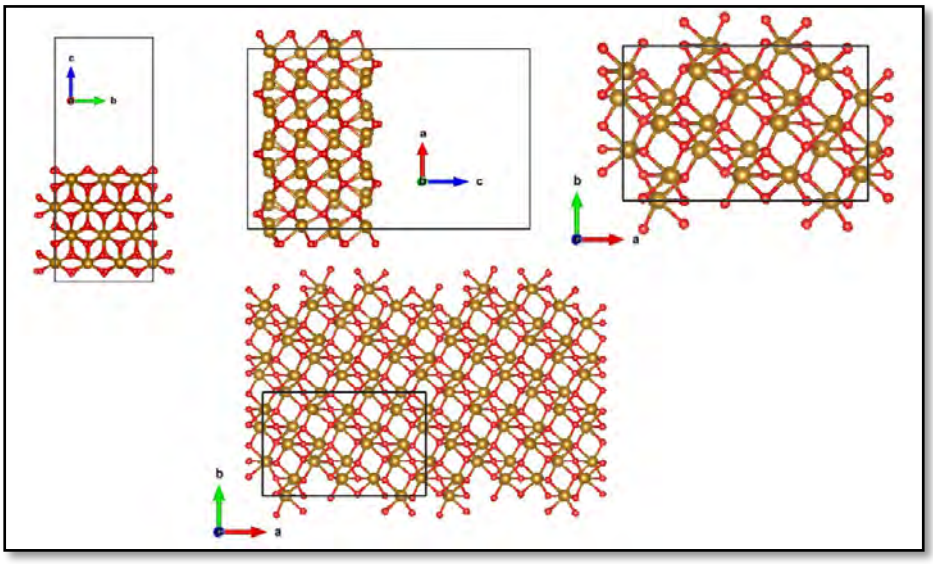

Figure-SI- 5. (top) Different views of the pristine hematite 110 surface (48 Fe, 72 O; hexagonal representation) used in DFT calculations. (bottom) an extended view with using periodic boundary conditions.

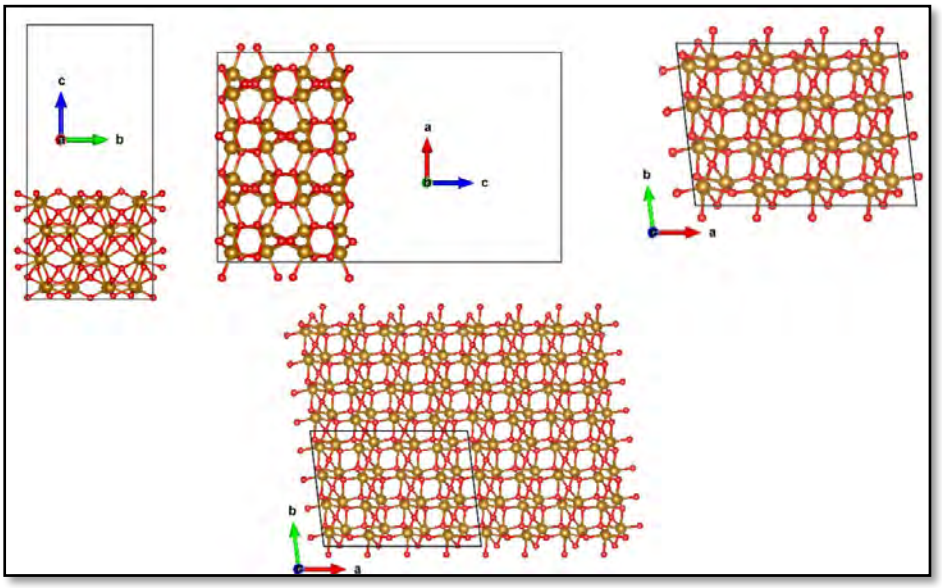

Figure-SI- 6. (top) Different views of the pristine hematite 110 surface (64 Fe, 96 O; rhomobohedral representation) used in DFT-MD calculations. (bottom) an extended view with using periodic boundary conditions.